Journal of Computational Physics **182,** 118–148 (2002)
doi:10.1006/jcph.2002.7154

Implementation of the Variational Riemann Problem Solution for Calculating Propagation of Sound Waves in Nonuniform Flow Fields

Igor Men'shov and Yoshiaki Nakamura

Department of Aerospace Engineering, Nagoya University, Nagoya 464-8603, Japan
E-mail: menshov@nuae.nagoya-u.ac.jp, nakamura@nuae.nagoya-u.ac.jp

Received July 10, 2001; revised May 29, 2002

The variational Riemann problem (VRP) is defined as the first variation of the solution to Riemann's initial-value problem, also known as the problem of breakup of an arbitrary discontinuity in a gas, when the initial data undergo small variations. We show that the solution to the VRP can be analytically obtained, provided that the solution to the baseline Riemann problem is known. This solution describes the interaction of two abutting parcels of small disturbances against the background of a given base flow and therefore can be efficiently implemented in numerical methods for aeroacoustics. When the spatial distribution of disturbances and base flow parameters are given at a time moment at mesh points of a computational grid, one can exactly determine the disturbance evolution for a short lapse of time by solving the VRP at mesh interfaces. This can then be applied to update disturbance values to a new time moment by using the standard finite-volume scheme. In other words, the VRP can be used in computational aeroacoustics in the similar way to the Riemann problem used in Godunov-type methods for computational fluid dynamics. The present paper elaborates on this idea and adopts the solution to the VRP as a building block for a finite-volume Godunov-type method for aeroacoustics.

Key Words: aeroacoustics; variational Riemann problem; Godunov-type numerical method.

1. INTRODUCTION

The present paper addresses the development of a novel numerical method for calculating propagation of sound waves in a nonuniform moving fluid. This method can be treated as an extension to the Godunov method [1], a well-known approach in computational fluid dynamics that efficiently employs the exact solution to Riemann's initial-value problem (RP) to approximate the numerical flux function at mesh interfaces. The RP, also referred

0021-9991/02 $35.00

to as the problem of the breakup of an arbitrary discontinuity in a gas, is the Cauchy problem for gas dynamics equations with initial distributions of gas parameters which are constant in space everywhere except for a surface, say $x = 0$, where they have a finite gap or discontinuity. A remarkable property of the RP is that it has a unique solution which can be analytically obtained for any physically feasible initial data. The most general description of this solution was given by Kochin [2].

From the physical point of view, the solution to the RP exactly represents the resultant flow arising from the interaction of two abutting uniform flows. Godunov first applied this solution to compute compressible flows. According to his original idea, the instantaneous state of the real flow, characterized by piecewise-smooth distributions of gas dynamics parameters, is approximately replaced by a set of elementary flows, which are uniform within each cell of the computational grid. These are then advanced in time by using the solutions to Riemann problems at cell interfaces between neighboring cells. In light of this approach the real flow evolution during a small lapse of time is treated as a result of numerous interactions of elementary uniform flows. The numerical method based on this consideration is a finite-volume method where the interface flux is evaluated through the RP solution. The major merit of this method is that it is perhaps a unique numerical method based in large part on the physics embedded in the compressible flow equations.

In the present paper we extend the philosophy of Godunov's approach to acoustic problems that treat sound wave propagation in a compressible, nonuniform, moving fluid. Following Godunov's suggestion, the instantaneous state of the acoustic field at a certain time moment is represented by a set of elementary disturbances uniformly distributed within each cell of the computational grid. Then, the subsequent evolution of the acoustic field for a small lapse of time can be thought of as a result of interactions between these elementary cell disturbances in a way similar to that of Godunov's method for compressible flows. To make this analogy complete, a powerful tool like the RP is needed to describe the interaction of two elementary disturbances.

We propose an extension to the RP as such a tool, which will henceforth be referred to as the *variational Riemann problem* (VRP). This can be mathematically defined as the problem on the first variation of the RP solution with respect to small variations in the initial data. Physically, this problem describes the process of interaction between two abutting uniformly distributed fields of disturbances against the background of the "breakup-discontinuity" base flow. The solution to the VRP yields the resultant disturbance field of this interaction. Therefore, similarly to the RP in Godunov's method for fluid dynamics, the solution to the VRP can be implemented in a finite-volume numerical model for calculating the propagation of sound waves in a nonuniform compressible medium.

Sound generation and propagation are very complicated processes governed by the compressible Navier–Stokes equations, which can be investigated by direct numerical simulation methods. For example, Mitchell, *et al.* [3] presented simulations of the sound irradiated by co-rotating vortices, Inoue and Hattori [4] investigated sound waves generated by shock–vortex interaction, Nakamura and co-workers [5, 6] and Loh *et al.* [7] simulated the near-field noise of an underexpanded supersonic jet with a shock cell structure. However, direct sound calculation for flows of practical interest at relatively high Reynolds numbers and usually moderate Mach numbers is quite expensive in terms of computer time.

Another common approach, which gives a significant computational savings over the direct numerical simulations, is based on the concept of linearization. In this approach, the flow field is decomposed into two constituents. One represents the field of a base or

mean flow characterized by averaged flow parameters. The other is the field of acoustic perturbations, the magnitude of which is assumed to be much smaller than that of the base flow. Commonly, the base flow is supposed to be known by another method: experimental, analytical, or numerical. The evolution of the perturbation field is solved by the model of linearized Euler's equations (LEE) that neglects both viscosity and nonlinear effects [8–10]. A shortcoming of the standard LEE model is that the resultant linearized equations no longer have a conservative form; therefore special attention should be given to numerical algorithms and boundary conditions to handle wave-type solutions correctly [11].

The numerical method developed in the present paper is based on the same principles as the standard LEE model, i.e., splitting the flow field variables into a mean flow and a perturbation part, and neglecting nonlinear and viscous terms. However, the present method differs from the conventional ones in the linearization procedure; that is, it is applied to discretized equations, not the differential ones. This means that the governing equations are first discretized in space and then linearized with respect to conservative variables of the base flow, so that the discretized perturbation equations are acquired in the form of conservation laws. The solution to the VRP is effectively exploited in this approach to linearize Godunov's numerical flux function and obtain relevant acoustic fluxes.

The paper is organized as follows. The statement and solution of the VRP are discussed in Section 2. Section 3 considers the proposed linearized methodology for obtaining Godunov's LEE discrete model. In Section 4, the treatment of boundary conditions by means of appropriate VRP solutions is discussed. Validation of the present method against the theoretical data available from several aeroacoustic theories is presented in Section 5. Some applications related to the problems of scattering and shock–sound wave interaction are presented in Section 6 before concluding the paper.

2. VARIATIONAL RIEMANN PROBLEM

Riemann's initial-value problem for one-dimensional extended gas dynamics equations,

$$\frac{\partial \mathbf{Q}}{\partial t} + \frac{\partial \mathbf{F}}{\partial x} = 0, \tag{1}$$

where $\mathbf{Q}$ and $\mathbf{F}$ are the conservative state vector and the flux vector, defined by

$$\begin{aligned} \mathbf{Q} &= (\rho, \rho u, \rho v, \rho w, \rho E)^T, \\ \mathbf{F} &= (\rho u, \rho u^2 + p, \rho uv, \rho uw, \rho H)^T, \end{aligned} \tag{2}$$

is formulated as a Cauchy problem with piecewise-constant initial data at $t = 0$:

$$\mathbf{Q} = \begin{cases} \mathbf{Q}_l & \text{for } x < 0, \\ \mathbf{Q}_r & \text{for } x > 0. \end{cases} \tag{3}$$

Here ρ, p, E, and H are the density, the pressure, the total energy, and the total enthalpy, and u, v, w are x, y, and z components of the velocity vector, respectively. Initial state vectors $\mathbf{Q}_l$ and $\mathbf{Q}_r$ are constant with respect to the space coordinate x.

This problem always has a unique solution under any physically allowable initial data, which is represented by a piecewise-analytical function of the self-similar parameter

$\lambda = x/t$ and initial state vectors $\mathbf{Q}_l$ and $\mathbf{Q}_r$ [2, 12]. Denoting this function by $\mathbf{Q}^R$, we can write the solution to the RP as

$$\mathbf{Q}(t, x) = \mathbf{Q}^R(\lambda,\ \mathbf{Q}_l,\ \mathbf{Q}_r). \tag{4}$$

It can also be proven (see Chapter 4 of [12], for example) that this solution necessarily has a fixed structure or wave pattern, no matter what the initial values are. This structure is characterized by the following flow features. First, these encompass a set of weak and strong discontinuities or waves produced by the breakup of an initial discontinuity at $x = 0$, which propagate at constant velocities ($\lambda = const.$). Among these waves, one and only one contact discontinuity (CD) must exist. It separates the gas located initially at $x < 0$ from that at $x > 0$. Second, uniform flow domains referred to as contact zones must exist, which abut the CD on both the left- and right-hand sides. The pressure and the x-directional velocity component have the same values in these zones. Third, the contact zone and the nonperturbed zone of the uniform initial flow on each side of the CD have to be separated by either only one shock wave or only one centered self-similar rarefaction wave, i.e., a Taylor wave (TW). Thus, the total number of waves in the RP solution is in the range from 3 to 5, and the entire flow domain at each time moment consists of several subdomains separated by the waves, where either uniform flows (in contact and nonperturbed zones) or TW flows are realized. The solution varies continuously through the TW region in accordance with the relations

$$u \pm a - \lambda = 0, \quad cu' \mp p' = 0, \quad v' = w' = s' = 0, \tag{5}$$

where a is the sound velocity, $c = \rho a$, s is the entropy, and the prime denotes the derivative with respect to λ. The upper sign in the relations (5) is used for the TW produced on the right-hand side of the CD, and the lower one is for the left-hand side.

Flow parameters in these subdomains are matched by appropriate relations between flow parameters, which are continuity relations at weak discontinuities, i.e., the first and last characteristics of the TW fan, or Rankine–Hugoniot relations at shock waves, or continuity of the pressure p and the velocity u at the CD. These relations just suffice to determine the wave pattern and the flow parameters in two contact zones. A more detailed description of the RP problem solution can be found in [12].

An extension of the RP, the VRP, can be suggested as follows. Let the solution to the RP, $\mathbf{Q}^R(\lambda, \mathbf{Q}_l, \mathbf{Q}_r)$, be known for initial state vectors $\mathbf{Q}_l$ and $\mathbf{Q}_r$. The question to be considered is how this solution varies when the initial parameters undergo small variations

$$\mathbf{Q}_l \to \mathbf{Q}_l + \delta\mathbf{Q}_l, \quad \mathbf{Q}_r \to \mathbf{Q}_r + \delta\mathbf{Q}_r. \tag{6}$$

This is specified by the first variation of the RP solution with respect to the initial state vectors, which can be represented by a linear form as

$$\delta\mathbf{Q}^R = M_l\delta\mathbf{Q}_l + M_r\delta\mathbf{Q}_r \tag{7}$$

in terms of two variational matrices, M_l and M_r, associated with the left- and right-hand side initial state vectors, respectively, and defined by the following relations:

$$M_i = M_i(\lambda, \mathbf{Q}^R) = \frac{\partial\mathbf{Q}^R}{\partial\mathbf{Q}_i}, \quad i = l, r. \tag{8}$$

The VRP is to determine the first variation of the RP solution $\mathbf{Q}^R$ or the variational matrices that define this variation. Note that in a manner similar to how the RP solution describes the interaction of two uniform compressible flows, the solution to the VRP does the same for small disturbances. Therefore, this is of prime importance for understanding the physics of the evolution of acoustic fields in nonuniform flows.

To solve the VRP, first note that both M_l and M_r are piecewise-analytical matrix functions of the self-similar parameter λ with the same domains of analyticity as the base nonvaried solution $\mathbf{Q}^R$. The analyticity domains are specified by the set of waves stemming from the initial discontinuity, or in other words, by the wave pattern produced in the nonvaried RP.

Moreover, these matrices are just constant with respect to λ within uniform flow subdomains, which are contact and nonperturbed zones of the nonvaried solution. Let $\lambda_1, \ldots, \lambda_5$ denote wave velocities, where λ_3 is the CD velocity and λ_1 and λ_2 are the velocities of the first and last characteristics in the TW, respectively, if $\lambda_1 \neq \lambda_2$, or the velocity of a shock wave or a weak discontinuity on the left-hand side of the CD, if $\lambda_1 = \lambda_2$. The notations λ_5 and λ_4 are used for the similar waves on the right-hand side. Then the variational matrices within nonperturbed regions are simply evaluated as

$$\begin{aligned} &M_l = I \quad \text{and} \quad M_r = O \quad \text{if } -\infty < \lambda < \lambda_1, \\ &M_l = O \quad \text{and} \quad M_r = I \quad \text{if } \lambda_5 < \lambda < +\infty, \end{aligned} \tag{9}$$

where I is the unit matrix and O is the null matrix.

In contact zones with $\lambda_2 < \lambda < \lambda_3$ and $\lambda_3 < \lambda < \lambda_4$, these matrices have to be defined by means of appropriate matching relations for perturbations at the CD $\lambda = \lambda_3$ and at the last characteristic in the TW, the shock wave, or the weak discontinuity $\lambda = \lambda_{2,4}$ as well.

We find it convenient to define the vector of primitive variables $\mathbf{U} = (u, p, s, v, w)^T$ and consider variational matrices μ_l and μ_r associated with this vector such that

$$\delta\mathbf{U}^R = \mu_l \delta\mathbf{U}_l + \mu_r \delta\mathbf{U}_r. \tag{10}$$

Once these matrices are determined, the variational matrices M_l and M_r can be obtained by the relation

$$M_i = B(\mathbf{U}^R)\mu_i B(\mathbf{U}_i)^{-1}, \quad i = l, r, \tag{11}$$

where $B(\mathbf{U})$ is the transforming Jacobian from the conservative to the primitive variables, defined by $B(\mathbf{U}) = \partial\mathbf{Q}/\partial\mathbf{U}$.

2.1. Solution in the TW Region

Solution of the VRP in the TW region with $\lambda_1 \leq \lambda \leq \lambda_2$ and $\lambda_4 \leq \lambda \leq \lambda_5$ is attained by varying the relations (5). This results in a system of ordinary differential equations for variations, which can be efficiently integrated in terms of two varied Riemann invariants $\delta I^{\pm}$ defined by

$$\delta I^{\pm} = c\delta u \pm \delta p. \tag{12}$$

Using matching relations at TW leading characteristics of

$$\begin{aligned} &\delta\mathbf{U} + \mathbf{U}'\delta\lambda_1 = \delta\mathbf{U}_l \quad \text{at } \lambda = \lambda_1, \\ &\delta\mathbf{U} + \mathbf{U}'\delta\lambda_5 = \delta\mathbf{U}_r \quad \text{at } \lambda = \lambda_5, \end{aligned} \tag{13}$$

yields relations for variations in the TW region,

$$\begin{aligned} \delta I^{\mp} &= \frac{c}{c_i}\delta I_i^{\mp} \mp c\int_{p_i}^{p}\frac{1}{c^2}\left(\frac{\partial c}{\partial s}\right)_p dp\cdot\delta s_i,\\ \delta u \pm \delta a &= 0,\\ \delta v &= \delta v_i,\\ \delta w &= \delta w_i,\\ \delta s &= \delta s_i, \end{aligned} \tag{14}$$

where the subscript $i = l$ and the upper sign are used for the left-hand-side TW, while $i = r$ and the lower sign are used for the right-hand-side TW. The variation of the leading characteristic velocity is simply determined by

$$\delta\lambda_i = \delta u_i + \delta a_i = \delta u_i + \left(\frac{\partial a}{\partial s}\right)_{p,i}\delta s_i + \left(\frac{\partial a}{\partial p}\right)_{s,i}\delta p_i. \tag{15}$$

Relations (14) can be transformed into a matrix form as

$$\delta\mathbf{U} = \mu_i^{\mathrm{TW}}\delta\mathbf{U}_i \tag{16}$$

with the matrix μ_i^{TW} defined by

$$\mu_i^{\mathrm{TW}} = \begin{vmatrix} 1-\Gamma & \mp(1-\Gamma)/c_i & \mp[\omega(1-\Gamma)+\Gamma(\partial a/\partial s)_p] & 0 & 0\\ \mp\Gamma c & c\Gamma/c_i & c\Gamma[\omega-(\partial a/\partial s)_p] & 0 & 0\\ 0 & 0 & 1 & 0 & 0\\ 0 & 0 & 0 & 1 & 0\\ 0 & 0 & 0 & 0 & 1 \end{vmatrix}, \tag{17}$$

so that the variational matrices in the TW regions take the form

$$\begin{aligned} &\mu_l = \mu_l^{\mathrm{TW}}, \quad \mu_r = O \qquad \text{for } \lambda_1 \le \lambda \le \lambda_2,\\ &\mu_l = O, \qquad \mu_r = \mu_r^{\mathrm{TW}} \quad \text{for } \lambda_4 \le \lambda \le \lambda_5. \end{aligned} \tag{18}$$

Here the following notation was used:

$$\begin{aligned} \Gamma &= \frac{2}{\gamma+1},\\ \gamma &= 1+\rho\left(\frac{\partial a^2}{\partial p}\right)_s,\\ \omega &= \int_{p_i}^{p}\frac{1}{c^2}\left(\frac{\partial c}{\partial s}\right)_p dp. \end{aligned} \tag{19}$$

For a calorically perfect gas, γ reduces to the ratio of specific heats, and ω and $(\partial a/\partial s)_p$ take the forms

$$\begin{aligned} \omega &= \frac{a-a_i}{(\gamma-1)s_i},\\ \left(\frac{\partial a}{\partial s}\right)_p &= -\frac{a}{2s_i}. \end{aligned} \tag{20}$$

Note that the convention about the usage of the subscript i and "plus–minus" superscript to distinguish left- and right-hand-side TWs is used in relations (15)–(20) as well.

2.2. Solution in Contact Zones

Variations of flow parameters are constant within two contact zones with $\lambda_2 \le \lambda \le \lambda_3$ and $\lambda_3 \le \lambda \le \lambda_4$, respectively, which must be defined by appropriate matching conditions for the waves bordering these zones. These conditions depend on the specific wave pattern exhibited by the solution of the base RP. Therefore, there are three distinguishing cases: The contact and unperturbed zones can be separated by (1) a weak discontinuity, (2) a TW, or (3) a shock wave.

In the case of weak discontinuity separation, or TW separation, matching relations can be uniformly written as

$$[\delta I^{\mp}] = [s] = [v] = [w] = 0 \quad \text{at } \lambda = \lambda_i, \tag{21}$$

where $[\cdot]$ denotes the magnitude of discontinuity at $\lambda = \lambda_i$. Here λ_i is assumed to equal λ_2 or λ_4, depending on which contact zone, on the left- or right-hand side, is under consideration, and the aforementioned double-sign superscript convention is used; i.e., the upper sign corresponds to the waves located on the right-hand side of the CD, while the lower one corresponds to the left-hand side waves.

Equations (21) are fewer in number than the unknowns; thus they are not sufficient to determine all components of the variational vector $\delta\mathbf{U}$ in the contact zone. There is indeterminacy of just one parameter; therefore this vector can be expressed as a one-parameter solution with one arbitrary or free parameter. In what follows, we find it convenient to write this in terms of initial variations $\delta\mathbf{U}_{l,r}$ as

$$\mathbf{U}_3^i = N^i \delta\mathbf{U}_i + \mathbf{m}^i C_i, \quad i = l, r \tag{22}$$

with matrix N and vector $\mathbf{m}$, which are referred to as contact matrix and vector, respectively, and free parameter C. Hereafter, the subscript 3 denotes contact zone values.

By taking δu_3 as the free parameter C and using relations (16) and (17) for TW variations, it can be shown that the contact matrix and vector in the case of TW separation are similar to those in the case of weak discontinuity separation. These are written for the both cases in the following form:

$$N^i = \begin{vmatrix} 0 & 0 & 0 & 0 & 0 \\ \mp c_3 & c_3/c_i & c_3(\omega_3 - \omega_i) & 0 & 0 \\ 0 & 0 & 1 & 0 & 0 \\ 0 & 0 & 0 & 1 & 0 \\ 0 & 0 & 0 & 0 & 1 \end{vmatrix}, \quad \mathbf{m}^i = \begin{vmatrix} 1 \\ \pm c_3 \\ 0 \\ 0 \\ 0 \end{vmatrix}. \tag{23}$$

The variation of the velocity of the TW's trailing characteristic is related to the constant C as

$$\delta\lambda_i = \left. \frac{C_i - \delta u^{\mathrm{TW}}}{u'} \right|_{\lambda=\lambda_i}, \tag{24}$$

where the variation of the velocity in the TW zone, δu^{TW}, is defined by relations (16) and (17).

A shock wave separating the contact and nonperturbed zones is another possible wave configuration of the RP solution. In this case the base flow parameters have a jump at this wave, following the Rankine–Hugoniot relations. The matching relations between variations are attained by varying the Rankine–Hugoniot relations. These can be written in a matrix form as

$$[(A - \lambda_i I) B \delta \mathbf{U}] = \delta \lambda_i [\mathbf{Q}], \tag{25}$$

where A represents the Jacobian matrix of the flux $\mathbf{F}$, i.e., $A = \partial \mathbf{F} / \partial \mathbf{Q}$, and the square brackets denote the magnitude of the discontinuity at the shock wave; i.e., $[\cdot] = (\cdot)_3 - (\cdot)_i$ with $i = l$ or r, depending on whether $\lambda_i = \lambda_1 = \lambda_2$ or $\lambda_i = \lambda_4 = \lambda_5$, respectively.

As in the case of TWs or weak discontinuities, the number of shock wave matching relations (25) is not sufficient to determine all variations in the contact zone. These relations are solved under the indeterminacy of one arbitrary or free parameter. The solution can also be represented in the form of relation (22) with C_i as the free parameter. We found it convenient to introduce this parameter as

$$C_i = \left[\frac{1}{\rho}\right] \delta m_i + \frac{\delta \rho_i}{\rho_i^2} m_i, \tag{26}$$

where m_i denotes the mass flux across the shock wave; i.e., $m_i = \rho_i (u_i - \lambda_i) = \rho_3 (u_3 - \lambda_i)$. Based on such a choice, by tedious but not difficult algebra, one can obtain the contact matrix N and the vector $\mathbf{m}$ for the case of shock wave separation as

$$N^i = \begin{vmatrix} 1 & \left(1 + M_i^2\right)/m_i + \chi_2 & -m_i \sigma_i T_i - \chi_3 & 0 & 0 \\ 0 & -m_i \chi_2 & m_i \chi_3 & 0 & 0 \\ 0 & -\Delta_i/(m_i T_3) & T_i/T_3 & 0 & 0 \\ 0 & 0 & 0 & 1 & 0 \\ 0 & 0 & 0 & 0 & 1 \end{vmatrix}, \quad \mathbf{m}^i = \begin{vmatrix} -1 - \chi_1 \\ \chi_1 m_i \\ \Delta_i / T_3 \\ 0 \\ 0 \end{vmatrix}, \tag{27}$$

where $\Delta_i = u_3 - u_i$, $M_i = m_i / c_i$ is the shock wave Mach number, T is the temperature defined by the partial derivative of enthalpy with respect to entropy with pressure held constant, and $\sigma = (\partial T / \partial p)_s / T$. The parameters χ_1, χ_2, χ_3 included in relations (27) are

$$\chi_1 = \frac{2 + m_i \Delta_i \sigma_3}{M_3^2 - 1}, \quad \chi_2 = \frac{1 + M_i^2 + m_i \Delta_i \sigma_3}{m_i \left(M_3^2 - 1\right)}, \quad \chi_3 = m_i T_i \frac{\sigma_3 + \sigma_1}{M_3^2 - 1}, \tag{28}$$

where $M_3 = m_i / c_3$ is the relative Mach number of the flow in the contact zone just after the shock wave.

When deciding the free parameter C_i by Eq. (26), the variation of the shock wave velocity is performed as

$$\delta \lambda_i = \delta u_i + \frac{\rho_3}{\rho_3 - \rho_i} \left[C_i - \frac{\delta \rho_i}{\rho_3} (u_i - \lambda_i) \right]. \tag{29}$$

The solution in the contact zones, which is given by Eq. (22) with Eq. (23) or (27), is completely determined by specifying the free parameters C_l and C_r corresponding to the left- and right-hand sides of the CD, respectively. This can be fulfilled by means of

matching relations at the CD. There are just two such relations linking the pressure and velocity variations at $\lambda = \lambda_3$:

$$[\delta u] = 0, \quad [\delta p] = 0. \tag{30}$$

Specifically, by substituting Eq. (22) into Eq. (30), two equations are obtained to define C_l and C_r. By using these equations, the construction of the solution in the contact zones is completed.

Thus, if the solution to the base RP is known, variational matrices of the VRP can be found throughout the flow, i.e., for any value of λ, where $-\infty < \lambda < +\infty$, by means of Eq. (22) with Eq. (23) or (27), and with C_l and C_r defined by Eq. (30). This can be compactly arranged by introducing the concept of proper and associated values. A parameter is either proper or associated, depending on the value of the self-similar variable λ. For example, if it is evaluated so that λ pertains to the left-hand side of the CD, then the left-hand-side parameters are referred to as proper, and those of the right-hand side as associated, and vice versa. Denoting associated values by superscripted asterisks and initial values by subscripted zeroes, we can represent the variation of the RP solution in the form

$$\delta \mathbf{U} = \mu \delta \mathbf{U}_0 + \mu^* \delta \mathbf{U}_0^*, \tag{31}$$

with the proper and associated matrices μ and μ^* defined as

$$\begin{array}{llll} \mu = I, & \mu^* = 0 & \text{in the nonperturbed zone,} \\ \mu = \mu^{\mathrm{TW}}, & \mu^* = 0 & \text{in the TW zone,} \\ \mu = N + \mathbf{m} \times \mathbf{k}^*, & \mu^* = \mathbf{m} \times \mathbf{n}^* & \text{in the contact zone,} \end{array} \tag{32}$$

where μ^{TW} is the TW's variational matrix given by Eq. (17) and N and $\mathbf{m}$ are defined by Eq. (23), when the TW or weak discontinuity occurs in the base RP, separating the contact and nonperturbed zones, or by relations (27) and (28) when a shock wave is the separation. The vectors $\mathbf{n}$ and $\mathbf{k}$ in these relations are given by

$$\mathbf{n} = \frac{m_2 \mathbf{N}_1 - m_1 \mathbf{N}_2}{m_2 m_1^* - m_1 m_2^*}, \quad \mathbf{k} = \frac{m_1 \mathbf{N}_2^* - m_2 \mathbf{N}_1^*}{m_2 m_1^* - m_1 m_2^*}, \tag{33}$$

where $\mathbf{N}_1$ and $\mathbf{N}_2$ denote the first and the second row of the contact matrix N, respectively, while m_1 and m_2 are the first and the second component of the vector $\mathbf{m}$, respectively.

The free parameter C of the contact zone, which concerns the variation of wave velocities via relations (24), (26), or (29), is specified with the foregoing designations as follows:

$$C = (\mathbf{k}^*, \delta \mathbf{U}_0) + (\mathbf{n}^*, \delta \mathbf{U}_0^*). \tag{34}$$

As a particular case of the foregoing general solution, let us consider the VRP solution for a single contact discontinuity. In this situation, the wave configuration of the base RP solution consists of three waves: one contact discontinuity with $\lambda = \lambda_3$ and two weak discontinuities $\lambda = \lambda_1 = \lambda_2$ and $\lambda = \lambda_4 = \lambda_5$ situated on the left- and right-hand sides of the contact discontinuity, respectively. The proper and associated matrices are defined in the contact zones with relations (23), (32), and (33) in this case, which can be written in the

form

$$\mu = \begin{vmatrix} c_0/\bar{c} & \mp 1/\bar{c} & 0 & 0 & 0 \\ \mp c_0 \pm c_0^2/\bar{c} & 1 - c_0/\bar{c} & 0 & 0 & 0 \\ 0 & 0 & 1 & 0 & 0 \\ 0 & 0 & 0 & 1 & 0 \\ 0 & 0 & 0 & 0 & 1 \end{vmatrix}, \quad \mu^* = \begin{vmatrix} c_0^*/\bar{c} & \pm 1/\bar{c} & 0 & 0 & 0 \\ \pm c_0 c_0^*/\bar{c} & c_0/\bar{c} & 0 & 0 & 0 \\ 0 & 0 & 1 & 0 & 0 \\ 0 & 0 & 0 & 1 & 0 \\ 0 & 0 & 0 & 0 & 1 \end{vmatrix}, \tag{35}$$

where $\bar{c} = c_0 + c_0^* = c_l + c_r$, and the upper sign must be used for $\lambda > \lambda_3$, while the lower one holds for $\lambda < \lambda_3$. Specifically, this yields the resultant variation of pressure and velocity in the interaction zone ($\lambda_1 \le \lambda \le \lambda_5$) as

$$\begin{aligned} \delta u &= \frac{c_l \delta u_l + c_r \delta u_r - (\delta p_r - \delta p_l)}{\bar{c}}, \\ \delta p &= \frac{c_r \delta p_l + c_l \delta p_r - c_l c_r\,(\delta u_r - \delta u_l)}{\bar{c}}, \end{aligned} \tag{36}$$

which exactly agrees with the linearized RP solution introduced by Godunov *et al.* [12].

3. LEE-BASED GODUNOV METHODOLOGY

In this section, the foregoing VRP solution is applied to a linearized numerical approach for studying the evolution of the acoustic field against the background of a nonuniform flowfield. As in the model of the linearized Euler equations commonly used for aeroacoustics calculations, the fluid flow in the present approach is decomposed into a mean or base flow and a field of acoustic disturbances, the magnitude of which is assumed to be much smaller than that of the base flow. The base flow is prescribed with other numerical or analytical methods and unmodified by the disturbances, whereas the evolution of the disturbance field depends strongly on the base flow and is determined by linearized equations. The base flow might also be time dependent.

To obtain the linearized discrete equations, we make use of the compressible Navier–Stokes equations that are spatially discretized on a given computational grid with the finite-volume method,

$$\omega_i \frac{d\mathbf{q_i}}{dt} + \sum_\sigma s_\sigma T_\sigma^{-1} \mathbf{F}_\sigma = \sum_\sigma \mathbf{s}_\sigma \mathbf{g}_\sigma, \tag{37}$$

where $\mathbf{q_i}$ is the ith cell average value of the vector of conservative variables, ω_i is the ith cell volume, s_σ is the σth cell interface area, $\mathbf{F}_\sigma$ is the local one-dimensional inviscid flux averaged over the interface, $\mathbf{g}_\sigma$ is the interface-averaged viscous flux, and T_σ is the transforming matrix defined by the coordinates of unit vectors forming the local basis at the interface [13]. The summation in Eq. (37) is performed over all interfaces surrounding the ith cell. The approximation for the interface fluxes $\mathbf{F}_\sigma$ and $\mathbf{g}_\sigma$ is made so that they can be regarded as functions of cell-attributed values $\mathbf{q_i}$.

The discretized flow variables in (37) are then split into the base flow and disturbance constituents, which are denoted by the symbol of overline and hat, respectively,

$$\mathbf{q_i} = \bar{\mathbf{q}}_\mathbf{i} + \varepsilon \hat{\mathbf{q}}_\mathbf{i}, \tag{38}$$

where $\varepsilon \ll 1$.

With this decomposition the inviscid and viscous fluxes can be represented by three contributions as

$$\begin{aligned} \mathbf{F}_\sigma &= \bar{\mathbf{F}}_\sigma + \hat{\mathbf{F}}_\sigma + \tilde{\mathbf{F}}_\sigma, \\ \mathbf{g}_\sigma &= \bar{\mathbf{g}}_\sigma + \hat{\mathbf{g}}_\sigma + \tilde{\mathbf{g}}_\sigma, \end{aligned} \tag{39}$$

which correspond to a base flow flux of $O(1)$, a linear acoustic flux consisting of terms of $O(\varepsilon)$, and a nonlinear acoustic flux including terms of $O(\varepsilon^2)$ and higher. The latter is denoted by the tilde symbol in (39).

The linearized equations for disturbances are obtained by substituting the decomposition (38) and (39) into Eq. (37) and collecting terms with the same order in the parameter ε. In doing so, several assumptions [8, 9, 11, 14] are made. First, we assume that the base flow variables alone obey the discretized Navier–Stokes equations (37), and therefore all terms of $O(1)$ can be removed. Second, the viscous disturbance fluxes $\hat{\mathbf{g}}_\sigma$ and $\tilde{\mathbf{g}}_\sigma$ play no major role in the propagation of acoustic waves, and thereby they may be neglected. Third, the contribution from the nonlinear inviscid acoustic fluxes, which is mostly responsible for sound generation processes, may be arranged by a suitable volume source term, S, modelling the production of disturbances. This term is commonly built up from available experimental data or calculated results obtained with a direct numerical simulation (DNS) or under certain restrictions a large eddy simulation, as suggested in [10, 25], for example.

With the foregoing assumptions, the linearized model for the evolution of small disturbances against the background of a base flow is described by the following equations:

$$\frac{d\mathbf{q_i}}{dt} + \frac{1}{\omega_i} \sum_\sigma s_\sigma T_\sigma^{-1} \hat{\mathbf{F}}_\sigma = S_i. \tag{40}$$

The key point of the present approach is the approximation of the cell-interface acoustic flux $\hat{\mathbf{F}}_\sigma$, which depends on both the base flow and disturbance variables. We treat this flux from the standpoint of Godunov's approach as the resultant flux produced at the cell interface due to interaction between disturbance fields in the two neighboring cells. By introducing the cell-interface-transformed conservative vector $\mathbf{Q}$ with the relation $\mathbf{Q} = \mathbf{T}_\sigma \mathbf{q}$, the acoustic flux can be obtained through the foregoing solution to the VRP as

$$\hat{\mathbf{F}}_\sigma = A\big(\bar{\mathbf{Q}}_\sigma^R\big)\hat{\mathbf{Q}}_\sigma^R, \tag{41}$$

where $A(\mathbf{Q}) = \partial\mathbf{F}/\partial\mathbf{Q}$ is the Jacobian matrix of the local one-dimensional inviscid flux and $\bar{\mathbf{Q}}_\sigma^R = \bar{\mathbf{Q}}_\sigma^R(0, \bar{\mathbf{Q}}_i^\sigma, \bar{\mathbf{Q}}_{\sigma(i)}^\sigma)$ is the solution to the base RP stated at the cell interface with appropriate left- and right-hand-side base flow variables, $\bar{\mathbf{Q}}_i^\sigma$ and $\bar{\mathbf{Q}}_{\sigma(i)}^\sigma$, respectively. Here the subscript $\sigma(i)$ denotes the order number of the cell abutting the ith cell through the σth cell interface.

The vector $\hat{\mathbf{Q}}_\sigma^R$ in (41) is the solution to the VRP, which represents the variation of the base RP solution due to the presence of the disturbance field in the two abutting cells. This can be written by using variational matrices obtained in the previous section as

$$\hat{\mathbf{Q}}_\sigma^R = M_i\big(0, \bar{\mathbf{Q}}_i^\sigma, \bar{\mathbf{Q}}_{\sigma(i)}^\sigma\big)\hat{\mathbf{Q}}_i^\sigma + M_{\sigma(i)}\big(0, \bar{\mathbf{Q}}_i^\sigma, \bar{\mathbf{Q}}_{\sigma(i)}^\sigma\big)\hat{\mathbf{Q}}_{\sigma(i)}^\sigma, \tag{42}$$

where the superscript σ indicates the values of disturbance variables at the center of the cell interface.

A first-order scheme is attained, if a constant distribution in space is assumed for the disturbance variables within each computational cell, so that $\hat{\mathbf{Q}}_i^\sigma = \hat{\mathbf{Q}}_i$. There are many different ways to achieve higher order accuracy. In the present approach, a higher order accuracy scheme is realized by linearly reconstructing the primitive vector of disturbances inside each computational cell [15, 16]. By doing so, cell interface disturbance variables are determined by

$$\hat{\mathbf{U}}_i^\sigma = \hat{\mathbf{U}}_i + \left(\nabla \hat{\mathbf{U}}_i, \mathbf{r}_i^\sigma\right), \tag{43}$$

with $\mathbf{r}_i^\sigma$ being the radius vector from the center of the ith cell to the center of the σth interface. The gradients associated with cell centers can be computed by using the values of primitive disturbance variables in the surrounding cells with the method of least squares.

Using relations (41) and (42), the discretized equation (40) can be written in the convenient form

$$\begin{aligned} \frac{d\hat{\mathbf{q}}_i}{dt} &= \mathbf{R_i}(\hat{\mathbf{q}}), \\ \mathbf{R_i}(\hat{\mathbf{q}}) &= S_i - \frac{1}{\omega_i}\sum_\sigma s_\sigma T_\sigma^{-1} A\left(\bar{\mathbf{Q}}_\sigma^R\right)\left[M_i T_\sigma \hat{\mathbf{q}}_i^\sigma + M_{\sigma(i)} T_\sigma \hat{\mathbf{q}}_{\sigma(i)}^\sigma\right], \end{aligned} \tag{44}$$

where the vector of conservative variables at the cell interface, $\hat{\mathbf{q}}_i^\sigma$, is derived through the primitive vector defined by Eq. (43). These equations are then solved, using a low storage third-order Runge–Kutta scheme, which is implemented as

$$\begin{aligned} \hat{\mathbf{q}}_i^{(1)} &= \hat{\mathbf{q}}_i^n + \frac{1}{3}\Delta t \mathbf{R}_i(\hat{\mathbf{q}}^n), \\ \hat{\mathbf{q}}_i^{(2)} &= \hat{\mathbf{q}}_i^n + \frac{2}{3}\Delta t \mathbf{R}_i\left(\hat{\mathbf{q}}^{(1)}\right), \\ \hat{\mathbf{q}}_i^{(n+1)} &= \hat{\mathbf{q}}_i^n + \frac{1}{4}\Delta t \mathbf{R}_i(\hat{\mathbf{q}}^n) + \frac{3}{4}\Delta t \mathbf{R}_i\left(\hat{\mathbf{q}}^{(2)}\right), \end{aligned} \tag{45}$$

with Δt being the time step. This scheme is stable under the standard CFL condition, based on the largest absolute wave speed of the base flow.

4. TREATMENT OF BOUNDARY CONDITIONS

Within the framework of the present approach, various numerical boundary conditions for acoustic fluxes can be treated in a common way by using the solution to an appropriate VRP. From the foregoing consideration, it follows that, if a face of the ith cell, σ, is found to be a part of the outer boundary of the computational domain, only the neighbor vector of disturbances, $\hat{\mathbf{Q}}_{\sigma(i)}^\sigma$, must be specified to determine the relevant acoustic flux using relations (41) and (42). This specification is done, depending on which boundary becomes involved in the calculation. There are three types of outer boundaries to be considered.

The first type is referred to as an inlet boundary. It corresponds to the situation where a given disturbance, $\hat{\mathbf{Q}}^{\text{ext}}$, is forced to be embedded in the flow at the boundary. In this case, the neighbor vector of disturbances in the boundary VRP solution is taken as

$$\hat{\mathbf{Q}}_{\sigma(i)}^\sigma = \hat{\mathbf{Q}}^{\text{ext}}. \tag{46}$$

The second type is an outlet boundary. This models the situation when acoustic disturbances leave the computational domain with no reflection at the boundary. This is achieved by setting the neighbor vector of disturbances at the boundary such that the vector of the VRP solution given by (42) satisfies the condition

$$\hat{\mathbf{Q}}^{\sigma}_{\sigma(i)} = \hat{\mathbf{Q}}^{R}_{\sigma}. \tag{47}$$

This yields the boundary condition

$$\hat{\mathbf{Q}}^{\sigma}_{\sigma(i)} = \left[I - M_{\sigma(i)}\right]^{-1} M_i \hat{\mathbf{Q}}^{\sigma}_{i}. \tag{48}$$

Finally, the third type of boundary condition is introduced to simulate the interaction of acoustic waves with a rigid wall. In general, the wall may be in motion. It is also divided into a main motion to be related to the base flow and a small acoustic mode motion that affects the acoustic field only, such as the vibrating surface of a speaker, for example. By specifying a conservative vector $\hat{\mathbf{Q}}^{\text{wall}}$, which is equal to the cell-based vector $\hat{\mathbf{Q}}^{\sigma}_{i}$ in all variables except for velocity components that are replaced by appropriate components of the velocity of the wall acoustic motion, the boundary condition for this type can be written as

$$\hat{\mathbf{Q}}^{\sigma}_{\sigma(i)} = I^{*}\left(\hat{\mathbf{Q}}^{\sigma}_{i} - \hat{\mathbf{Q}}^{\text{wall}}\right) + \hat{\mathbf{Q}}^{\text{wall}}. \tag{49}$$

Here the matrix I^{*} coincides with the unit matrix I in all components other than $(I^{*})_{22}$, which is equal to -1.

5. VERIFICATION TESTS

In this section we present the results of three test calculations carried out to verify the present numerical approach and to examine the accuracy of the computational solutions. The first two problems deal with the acoustic fields generated in a quiescent gas by means of a monopole-type sound source and a dipole-type sound source, respectively. The third one is the problem of plane monochromatic sound waves incident on a plane shock wave. Each of these problems allows for a closed-form analytical solution that can be applied for comparison with relevant numerical solution to determine the accuracy of the proposed conceptual model.

5.1. Monopole-Type Emitter

The monopole-type source of sound waves is modeled with the emitter represented by a rigid sphere of radius R, which executes small harmonic radial pulsations in a gas at rest. The ambient gas is assumed to be a calorically perfect gas with base pressure p_0 and base density ρ_0. The radial velocity of points on the surface of the sphere is given as $U_r = U_0 \cos(\omega t)$, where t is time and ω is the frequency of pulsations. For the linearized model to be applicable, the characteristic velocity of pulsations, U_0, is supposed to be small compared with the speed of sound in the ambient gas.

The calculation of this problem is carried out in the computational domain bounded by the emitter surface and the outer spherical surface located at a distance of about 5 radii from the emitter. Although the problem is one dimensional, this calculation is performed

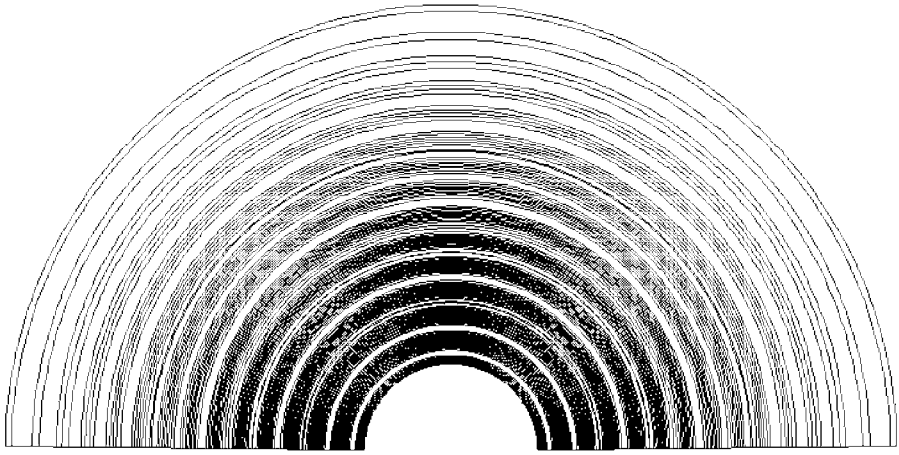

FIG. 1. Iso-contours of the acoustic pressure field for a monopole emitter ($Str = 10.82$).

in the meridional plane as axis-symmetric by using a structured grid that consists of 150 computational cells uniformly distributed along the emitter surface and 80 even cells in the radial direction. The emitter surface is treated by the wall-type boundary conditions considered in the previous section. The outlet boundary conditions are implemented at the outer boundary.

Computed results are represented here by instantaneous iso-contours of the acoustic pressure, which are shown in Fig. 1 for a high-frequency condition related to $Str = 10.82$. Here Str denotes the Strouhal number based on the emitter radius, the emitter frequency, and the speed of sound in the ambient gas; i.e., $Str = \omega R/c_0$. A centrally symmetric wave pattern of the computed acoustic field is clearly discernible in this figure.

A quantitative comparison is fulfilled for the total intensity of the irradiated sound field defined by

$$I = \oint \overline{\hat{p}\hat{v}_n}\, ds, \tag{50}$$

where the integration is performed over a spherical surface surrounding the emitter, $\hat{v}_n$ denotes the component of the acoustic velocity normal to this surface, and the overbar means time averaging.

According to acoustic theory [17], the normalized total emission depends on the Strouhal number and has the following

$$\frac{I}{I^*} = \frac{Str^2}{1 + Str^2}, \tag{51}$$

where I^* is a reference intensity given by $I^* = 2\pi R^2 c_0 \rho_0 U_0^2$.

In the calculation the total intensity of irradiated sound is computed by integrating the flux of sound energy $\hat{p}\hat{v}_n$ over the outer boundary and averaging the resultant value over the period of emitter oscillations. Calculations have been performed for different values of the Strouhal number, which correspond to low- and high-frequency emitters. In Fig. 2, the computed values of the normalized intensity of sound are plotted versus the Strouhal number.

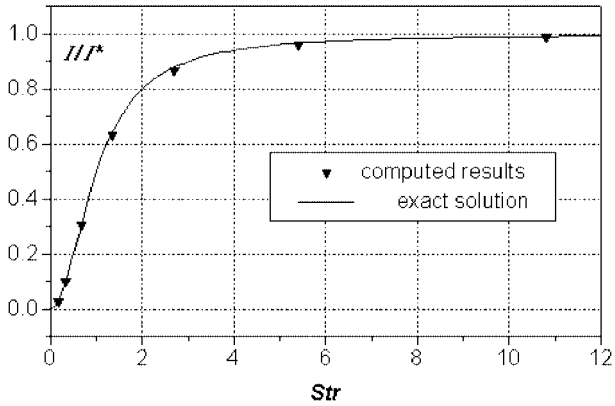

FIG. 2. Total sound intensity versus Strouhal number for monopole-type emitter.

For comparison, the theoretical relation (51) is also shown. As is seen from this figure, the computed data well agree with the theoretical curve over a wide range of wavelength.

5.2. Dipole-Type Emitter

The dipole-type source of sound waves is simulated in the same manner as the monopole-type source by moving a rigid sphere in a gas at rest. The acoustic field is generated by the sphere with radius R executing small harmonic translatory oscillations at a frequency of ω. Taking the direction of the oscillations as the x axis of a Cartesian system of coordinates, the velocity components of points on the sphere surface are then given as $U_x = U_0 \cos(\omega t)$, $U_y = U_z = 0$, where the velocity of the oscillations is also assumed to be small compared with the speed of sound in the ambient gas.

Calculation conditions for this test problem are similar to those of the monopole source. The computed results are shown in Fig. 3, where instantaneous iso-contours of the acoustic pressure field are plotted for a high-frequency dipole emitter with $Str = 10.82$. As can be

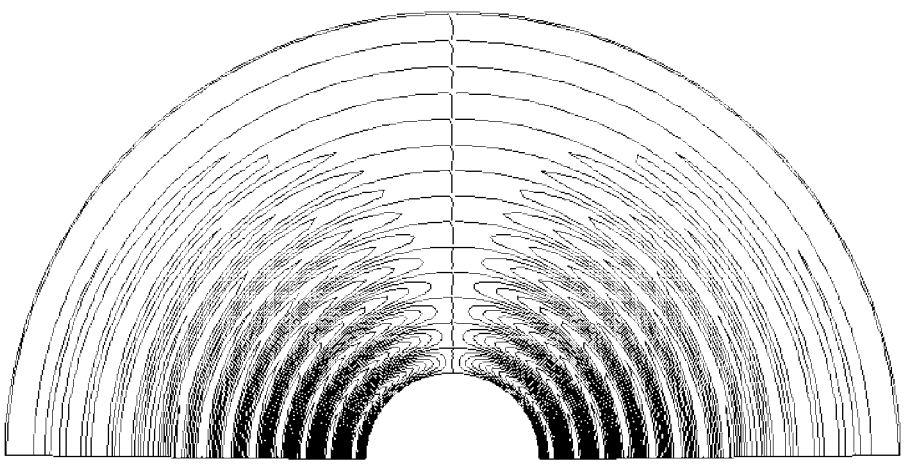

FIG. 3. Iso-contours of the acoustic pressure field for a dipole emitter ($Str = 10.82$).

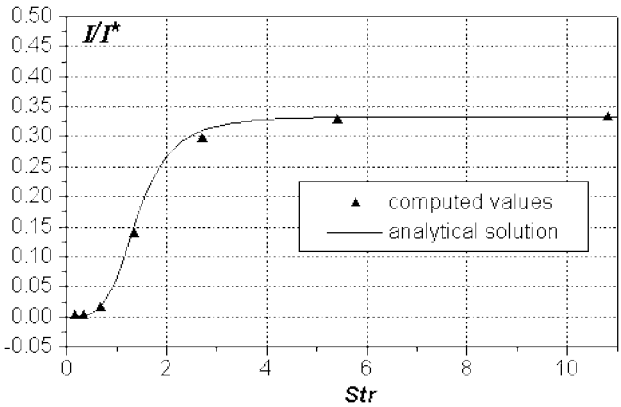

FIG. 4. Total sound intensity versus Strouhal number for dipole-type emitter.

seen, there are preferred emissions in the direction of emitter oscillations. The wave pattern is strictly symmetric with respect to the vertical meridional plane.

The computed total intensity of sound emission is presented in Fig. 4. Acoustic theory [17] predicts the total emission from the dipole source as

$$\frac{I}{I^*} = \frac{1}{3}\frac{Str^4}{4 + Str^4}. \tag{52}$$

As seen from the figure, the calculated results are in good agreement with the theory for the range of *Str*.

5.3. Sound Wave Incident on a Shock Wave

The third test to verify the present numerical method concerns the refraction of sound waves by a shock wave. Figure 5 shows a schematic drawing of the acoustic wave/fluid flow

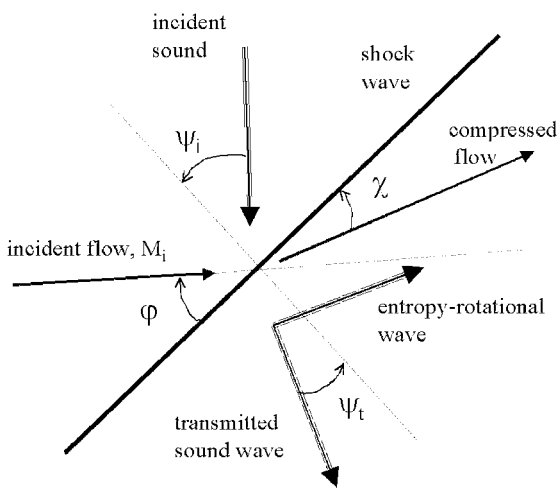

FIG. 5. Schematic drawing of sound–shock interference: M_i, incident flow Mach number; ϕ, impingement angle; χ, deflection angle; ψ_i, incident sound angle; ψ_t, transmitted sound angle.

configuration. This represents a steady oblique shock wave that is irradiated with planar monochromatic sound waves. The base flow comprises two uniform flows: an incident flow with Mach number M_i and incidence angle φ and a compressed flow behind the shock wave. The angle χ denotes the angle of flow deflection, which depends on M_i and φ through the Rankine–Hugoniot relations. Sound is incident on the shock wave from the side of the rarefied gas at angle ψ_i. Because the incident flow is supersonic, there must be no reflected waves formed in the incident flow ahead of the shock, while a transmitted wave with an angle of propagation ψ_t appears behind the shock along with an entropy-rotational wave that is carried by the gas flow.

This problem was first treated by Blokhintsev in 1945 for the case of normal incidence on a shock wave in an ideal gas. The analytical solution, cited in [17], yields parameters (transmission coefficients) of transmitted sound waves as a function of the Mach number of the incident flow. Then Brillouin tried studying oblique incidence but obtained incorrect results [18]. Kontorovich corrected these results and extended the solution to an arbitrary gas model [19].

By using the VRP solution described in Section 3, the solution to the sound–shock interference problem also can be efficiently obtained from appropriate proper and associated matrices. In fact, the transmitted field must satisfy the VRP solution with initial primitive disturbance vectors $\delta\mathbf{U}_i$ and $\delta\mathbf{U}_t$, where the subscript i denotes the incident wave parameters. Therefore, these must satisfy the relation

$$\delta\mathbf{U}_t = \mu_0\delta\mathbf{U}_i + \mu_0^*\delta\mathbf{U}_t, \tag{53}$$

where μ_0 and μ_0^* are proper and associated matrices in the contact zone behind the shock wave, which are given by (32) with the contact matrix M and the contact vector $\mathbf{m}$ being determined by (27).

This field consists of a transmitted adiabatic sound wave, $\delta\mathbf{U}_1$, and an entropy-rotational wave, $\delta\mathbf{U}_2$, such that

$$\delta\mathbf{U}_t = \delta\mathbf{U}_1 + \delta\mathbf{U}_2. \tag{54}$$

Parameters of the entropy-rotational wave obey the following relations:

$$\delta p_2 = 0, \quad (\delta\mathbf{v}_2, \mathbf{v}_{sh}) = 0. \tag{55}$$

The refraction law for the sound wave is formulated as

$$\frac{(\delta\mathbf{v}_i, \mathbf{k}_i) + a_i}{\sin\psi_i} = \frac{(\delta\mathbf{v}_1, \mathbf{k}_1) + a_{sh}}{\sin\psi_t}, \tag{56}$$

where $\mathbf{k}$ denotes the unit propagation vector and the subscript sh indicates parameters of the compressed flow behind the shock wave. Parameters of the sound wave are related as follows:

$$\delta s_1 = 0, \quad \delta p_1 = \rho_{sh}(a_{sh} + (\mathbf{k}_1, \mathbf{v}_{sh}))\delta v_1. \tag{57}$$

Equations (53)–(57) can be solved by using simple Newton's iterations. This determines the amplitudes of the transmitted sound and entropy-rotational waves. Figure 6 shows

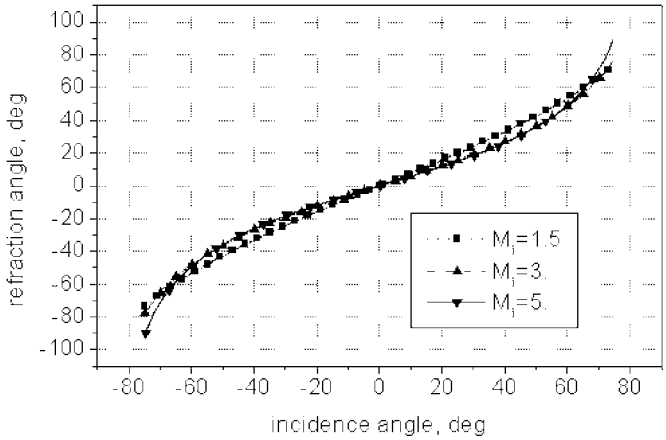

FIG. 6. Refraction angle versus incidence angle.

the refraction angle, ψ_t, versus the incidence angle, ψ_i, calculated with this approach for $\varphi = \pi/2$ and several values of the incident flow Mach number. The pressure ratio between the incident and transmitted waves scaled by M_i^2 is plotted versus the incidence angle in Fig. 7 for three values of M_i. These results are exactly in line with those obtained previously in [19].

The numerical simulation of a sound wave incident on a shock wave is performed on a two-dimensional structured grid in a rectangular computational domain. First, the case of normal incidence is considered, where the base flow is a gas flow upstream and downstream of a stationary plane shock wave vertically situated at the middle of the computational domain. The incident sound waves are modeled by inlet boundary conditions at the left boundary, where the primitive vector of disturbances is specified as $\hat{\mathbf{U}} = \hat{\mathbf{U}}_0 \cos(\omega t)$. The amplitude vector $\hat{\mathbf{U}}_0 = (\hat{p}_0/(\rho_i c_i), \hat{p}_0, 0, 0,)^T$, where $\hat{p}_0$ is the pressure amplitude of the wave. The nonreflecting boundary conditions described in Section 5 are used for other boundaries. There exist no disturbances in the computational domain at the initial instant.

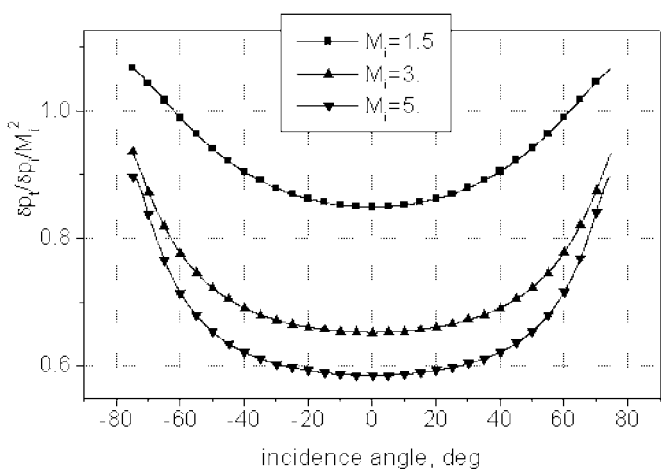

FIG. 7. Pressure amplification in the transmitted wave versus incidence angle.

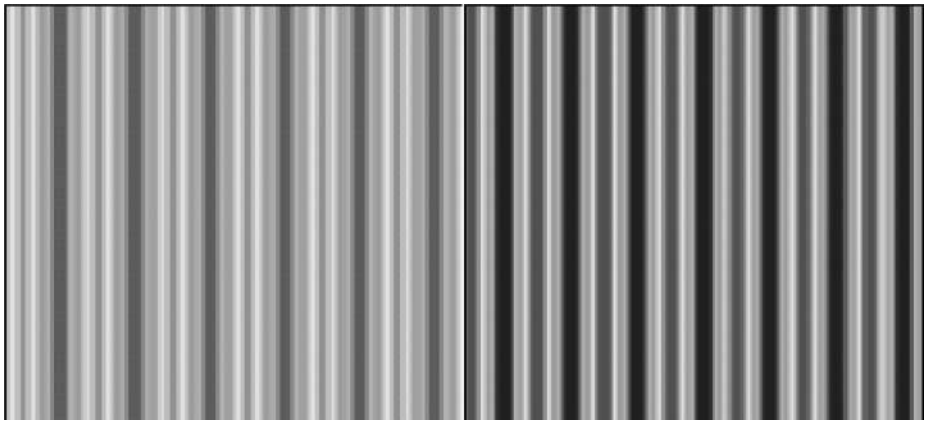

FIG. 8. Pressure contours in the normal incidence problem, where $\omega = 8\pi$, $\hat{p}_0 = 0.01$, and $M_{\text{sh}} = 1.5$.

Although the problem is substantially one dimensional, calculations are carried out as two dimensional on a grid with 320 and 10 cells evenly distributed in the streamwise and normal directions, respectively.

Calculated results for a nondimensional frequency, ω, of 8π, incident wave amplitude, $\hat{p}_0$, of 0.01, and a shock Mach number of 1.5 are plotted in Figs. 8 and 9, where the computed acoustic pressure is displayed in contours and as a streamwise distribution, respectively. Since the gas in the upstream region moves at supersonic speed, there must be no waves reflected from the shock. This is clearly observed in Fig. 9, where the waveform ahead of the shock is exactly in line with that specified at the inlet boundary. It can also be seen that there is no reflection of sound waves from the right boundary, although the downstream flow is subsonic.

While being transmitted across the shock, the pressure amplitude of the sound wave is increased. This increase is well captured by a calculation without any artificial overshoots or

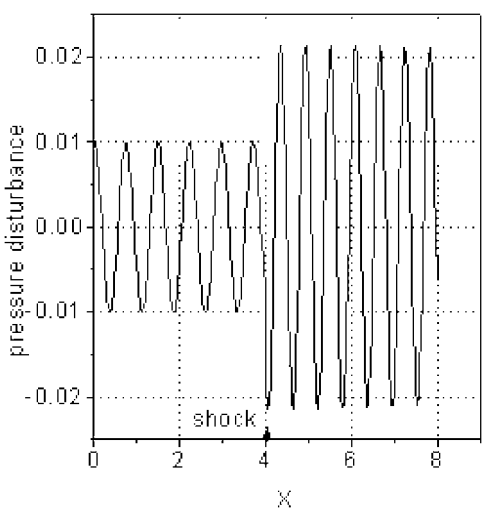

FIG. 9. Streamwise distribution of pressure in the normal incidence problem, where $\omega = 8\pi$, $\hat{p}_0 = 0.01$, and $M_{\text{sh}} = 1.5$.

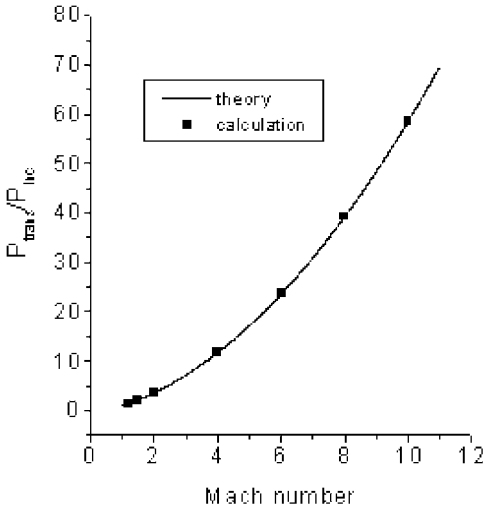

FIG. 10. Amplification of sound pressure for normal incidence of sound on shock.

undershoots for when the acoustic flux at the shock was computed inaccurately, or with some approximations. The pressure ratio of the incident wave to the transmitted one is plotted for several values of the shock wave Mach number in Fig. 10 along with the analytical solution given in [17] for comparison. The agreement between the computation and the theory is very good.

The numerical simulation of an oblique incidence of sound on a shock wave is also considered. This calculation is carried out in the computational domain taken such that its diagonal is in line with the shock wave. Thus, unlike the normal incidence case previously mentioned, the shock is no longer aligned with the grid lines.

The following simulation parameters were used: a uniform grid containing 300 and 200 cells in the horizontal and vertical directions, respectively, a Mach number of the rarefied flow before the shock of $M_i = 6$, and an impingement angle of $\varphi = 74.32^\circ$. Under these conditions, the compressed flow is deflected at $\chi = 40^\circ$.

The shock wave is irradiated by planar sound waves from the upstream side. This is modeled by setting the primitive vector of acoustic parameters at the left and top boundaries as

$$\hat{\mathbf{U}} = \hat{\mathbf{U}}_0 \cos[(\mathbf{k}, \mathbf{r}) - (\omega + (\mathbf{k}, \mathbf{V}_i))t], \tag{58}$$

where $\mathbf{k} = \omega \mathbf{n}/c_i$, with $\mathbf{n}$ being the unit propagation vector. The bottom and right boundaries of the computational domain are treated with outlet boundary conditions (48). There are no initial disturbances.

The angle of sound incidence, ψ_i, was taken to be 48.45°. In the flow conditions under consideration, the theory predicts that sound is refracted behind the shock wave at $\psi_t = 34.32^\circ$ (see Fig. 6), which corresponds to the propagation of transmitted sound waves just in the vertical direction toward the bottom boundary of the computational domain. This is clearly discernible in numerical results shown in Fig. 11, which displays contours of the computed sound pressure with $\omega = 7.5\pi$.

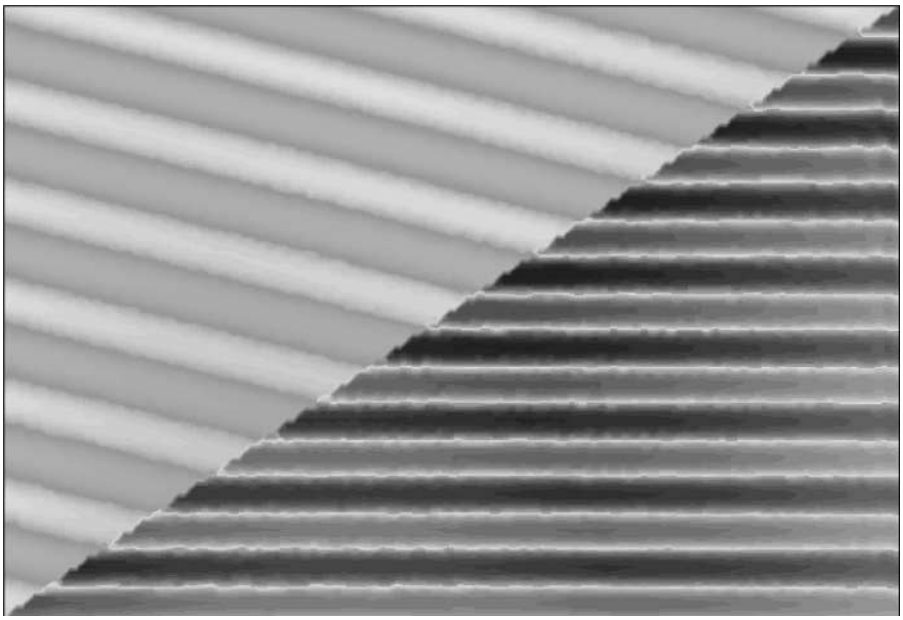

FIG. 11. Computed acoustic pressure field for oblique sound–shock incidence.

6. EXAMPLE CALCULATIONS

In this section we present the results of two example calculations carried out with the numerical approach proposed here. The problems involve propagation of acoustic disturbances against the background of a nonuniform base flow. As in previous verification calculations, it is also assumed here that the base flow is given and not affected by disturbances. A calorically perfect gas with a ratio of specific heats, γ, of 1.4 is used as the gas model.

6.1. Scattering of Sound Waves by a Vortex

The scattering of sound waves by a compressible vortex has been used as a test problem to validate numerical schemes for aeroacoustic calculations [20, 21]. This problem has been intensively studied during the past 20 years (for example, see [22] and references therein) and hence a large number of theoretical, numerical, and experimental results can be used for comparison.

We study the scattering problem by solving the discretized equations of the LEE model presented in Section 4. The computations are performed in a square computational domain with a side length $2L$, which is schematically drawn in Fig. 12. A plane sound wave with wavelength λ is emitted on the left side of the domain and propagates toward a two-dimensional vortex with a core radius of a, which is located in the center of the domain. Parameters of scattered sound are analyzed at the observation point specified by the magnitude of the radius r and the polar angle φ.

The distribution of the vortex flow parameters in the radial direction is taken so as to follow the two-dimensional compressible Euler equations. Specifically, we choose a zero circulation homentropic vortex [20], where the velocity of the base flow decays exponentially fast as we go away from the vortex center, and the entropy has a constant distribution

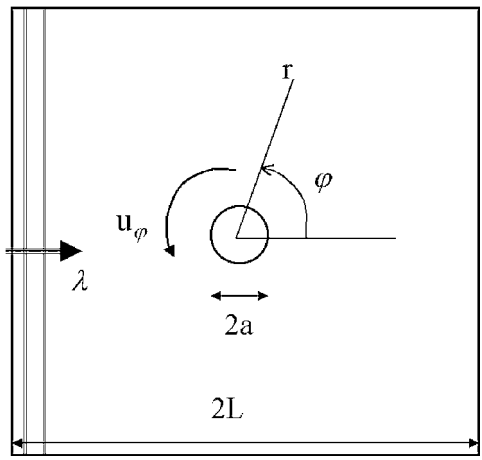

FIG. 12. Schematic diagram for sound scattering calculations.

in space:

$$\begin{aligned} u_r &= 0, \\ u_\varphi &= 2\frac{r}{a}\mu \exp\left[-\left(\frac{r}{a}\right)^2\right], \\ p &= const \cdot \rho^\gamma. \end{aligned} \tag{59}$$

The factor μ in these relations is proportional to the maximal value of the azimuthal velocity u_φ, which characterizes the vortex intensity. Under these asumptions, the pressure is given by

$$p = p_\infty \left\{1 - \frac{\gamma - 1}{\gamma}\frac{\rho_\infty}{p_\infty}\mu^2 \exp\left[-2\left(\frac{r}{a}\right)^2\right]\right\}. \tag{60}$$

The generation of incident sound waves at the left-hand boundary of the computational domain is modeled by the inlet boundary conditions with the prescribed primitive vector of disturbances taken as $\hat{\mathbf{U}}_\sigma = \hat{\mathbf{U}}_0 \cos \omega t$. The bottom, top, and right-hand boundaries are treated with the outlet boundary conditions. A two-dimensional structured grid is used, which consists of 271 evenly spaced cells in each direction. The computational domain extends 20 vortex core radii from the center; i.e., $L/a = 20$.

The scattered wave field is thought of as a field that arises from the interaction of the incident waves with the vortex flow field. Therefore, while computing the propagation of incident waves, scattered waves can be obtained by subtracting the acoustic field computed in the gas at rest, i.e., without the base flow ($\mu = 0$), from identical computations performed in the presence of the vortex flow.

Calculations are carried out for several values of two basic nondimensional parameters which strongly affect the scattering process. One of these parameters is the vortex Mach number, M_v, defined with the maximal velocity, $u_{\varphi,\max}$, and the speed of sound at infinity, c_∞. The other is parameter δ, which equals the ratio between the wavelength of incident waves and the vortex radius, i.e., $\delta = \lambda/a$. It is assumed that there is initially no acoustic

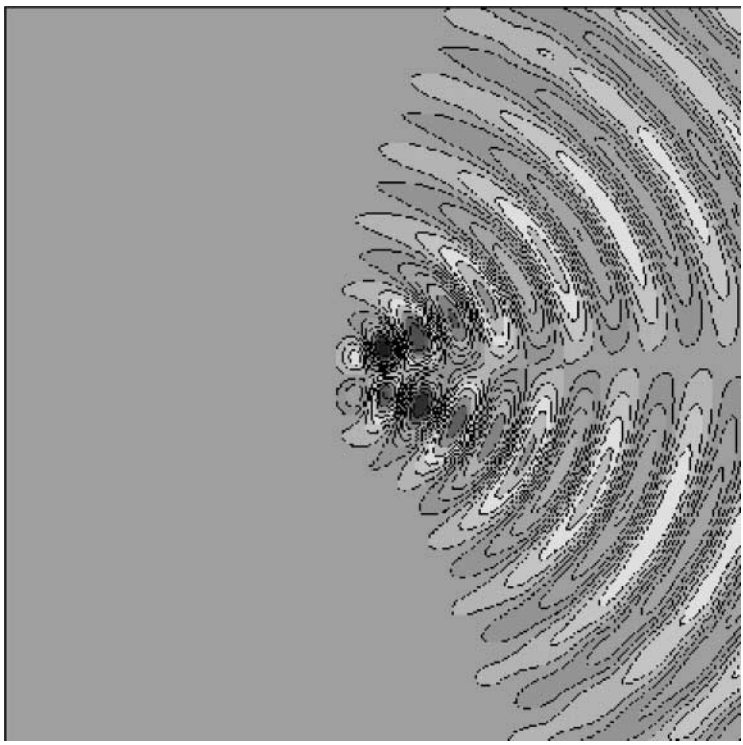

FIG. 13. Instantaneous pressure contours in the scattered field for $M_v = 0.125$ and $\delta = 4$.

field in the computational domain, and the acoustic source term S on the right-hand side of Eq. (44) is neglected.

Figure 13 shows instantaneous contours of the computed pressure in the scattered field for $M_v = 0.125$ and $\delta = 4$. As seen from this figure, forward scattering dominates over the backward one, and the maximum scattering is achieved in two directions which make angles of about $\pm 30^\circ$ with the direction of incident wave propagation. The root-mean-square pressure amplitude of the scattered waves, p_{rms}, is plotted as a function of φ for different values of r in Fig. 14. The pressure is normalized by the incident wave pressure amplitude p_0 and the factor $\sqrt{\lambda/r}$. According to the analysis given in [23], the scattering amplitude decays in the far field as $\sqrt{r}$. This is also attested to by the present calculations; the curves in Fig. 14 tend to collapse into a single curve as the ratio r/λ increases.

The foregoing results from the present approach agree well with the results obtained in [20], where the scattering of plane sound waves by a vortex has been investigated under similar conditions by direct computation of the compressible Navier–Stokes equations. The scattered field was also found in this research to prefer the direction of the incident wave propagation, where peak scattering occurs at about $\pm 30^\circ$ from the incident wave direction. In addition to this, the scattering was slightly asymmetrical with respect to the incident wave direction. Such asymmetry is clearly discernible in Fig. 14 as well. There is only a small discrepancy, which is within a few percent for the peak values of p_{rms}. This may be explained by the effect of the source term S that is neglected in the present calculations.

As the wavelength of the incident waves increases, the wave pattern of the scattered field changes qualitatively. The region where scattering waves travel extends toward the

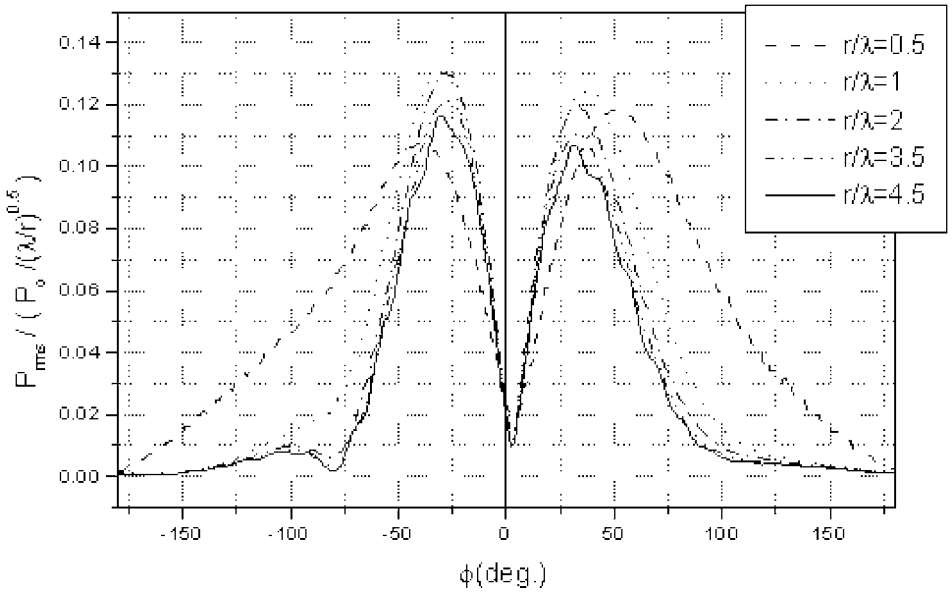

FIG. 14. Normalized root-mean-square pressure levels for $M_v = 0.125$ and $\delta = 4$.

backward direction. The backscatter phenomenon is intensified and becomes comparable with the forward scattering. For a low Mach number, a far-field approximation of the scattered field can be analytically obtained in the limit where the acoustic waves have long wavelength compared with the scale of the vortex. This is the so-called Born limit [24]. According to this analysis, the scattering of sound in the Born limit occurs in both forward and backward directions with a typical quadrupole directivity wave pattern.

The backscatter phenomenon for long-wave incident waves has also been supported by calculations performed with the present numerical model. As an example, in Fig. 15 we show instantaneous pressure contours of the scattered waves under the conditions of $M_v = 0.125$ and $\lambda/a = 10$. The scattered field directivity is evidently of quadrupole type. The distribution of the root-mean-square pressure versus the observation angle φ is plotted in Fig. 16 for increasing values of the radius. The pressure is again normalized by the factor $\sqrt{\lambda/r}$ to validate the $1/\sqrt{r}$ scaling in the far field.

These results show that there are preferred scatterings in two forward directions and two backward directions. Maximum scattering happens at polar angles of about $\pm 40^\circ$ and $\pm 130^\circ$. Overall, the backward scattering is about one-half the forward scattering. This agrees well with the results of the far-field Born limit analysis in [24]. The $1/\sqrt{r}$ decay of the scattered field in the far field is reached even at $r = 2\lambda$, as seen from Fig. 16, where all curves for larger radii show little deviation from that for $r = 2\lambda$. Note again that the scattering is found to be somewhat asymmetrical with respect to $\varphi = 0$.

Calculations for the cases of stronger vortex flows are displayed in Figs. 17 and 18, where the normalized values of p_{rms} are plotted as a function of the polar angle with radius as a parameter. Here, the incident sound wave has $\delta = 4$, and two vortex Mach numbers are chosen: $M_v = 0.25$ and $M_v = 0.8$. A trend toward a more asymmetric pattern in the scattered field is clearly seen as the vortex intensity increases. Thus, the scattering for

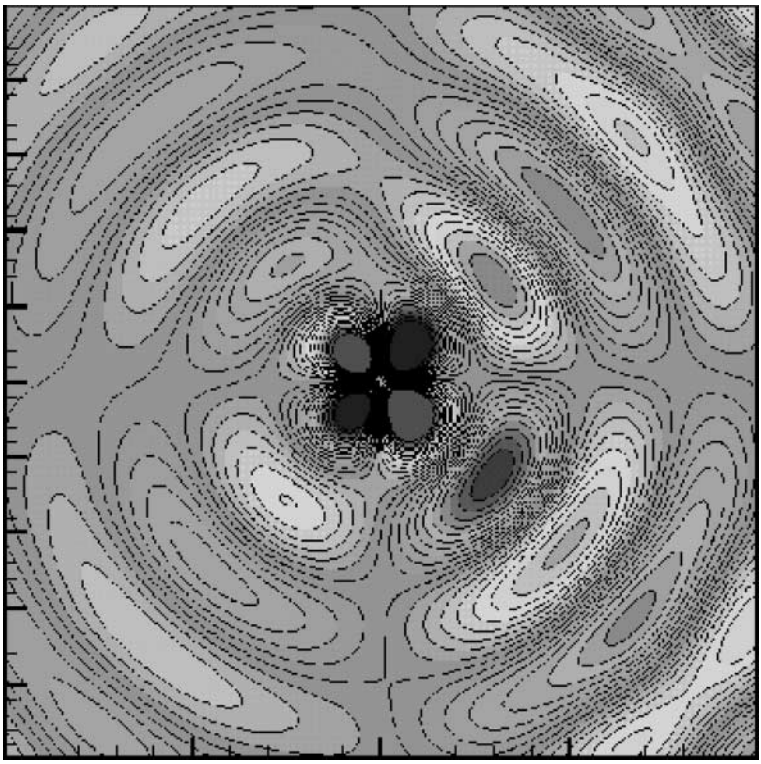

FIG. 15. Instanteneous contours of pressure in the scattered field for $M_v = 0.125$ and $\delta = 10$.

$M_v = 0.8$ occurs predominantly in the forward direction with a narrow angular sector, which is shifted in the direction of vortex swirling by about 25° from the incident wave direction. However, backward scattering also occurs in this case. This is in contrast to the case of low-Mach-number scattering, where it is negligible.

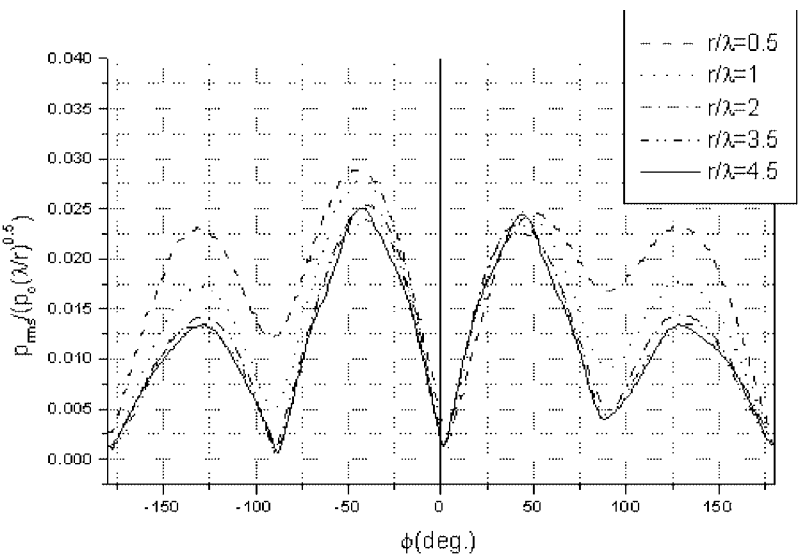

FIG. 16. Normalized root-mean-square pressure levels for $M_v = 0.125$ and $\delta = 10$.

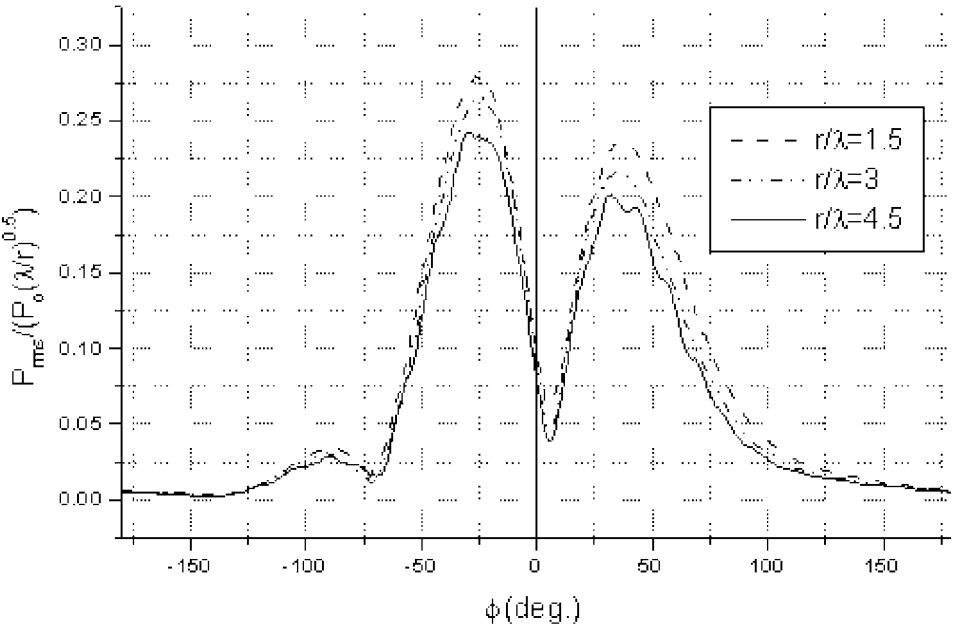

FIG. 17. Normalized root-mean-square pressure levels for $M_v = 0.25$ and $\delta = 4$.

In accordance with the far-field approximation [24], the scattered field is symmetric about the incident wave direction and the scattered pressure must vanish in the forward direction with $\varphi = 0$ when the vortex Mach number is small. However, the foregoing computational results exhibited asymmetric distributions and a finite scattering at $\varphi = 0$ as seen from

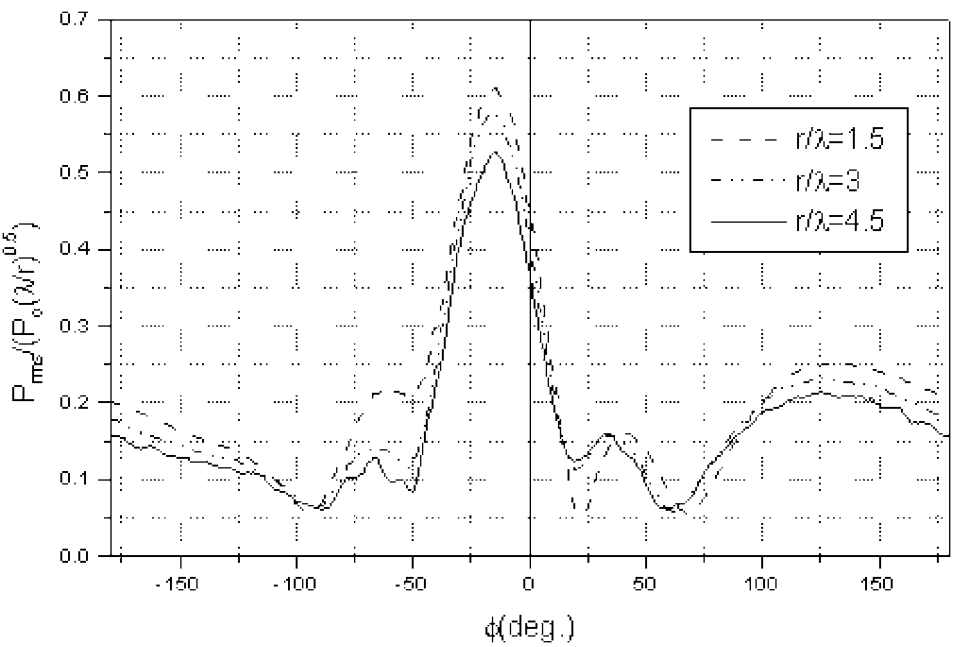

FIG. 18. Normalized root-mean-square pressure levels for $M_v = 0.8$ and $\delta = 4$.

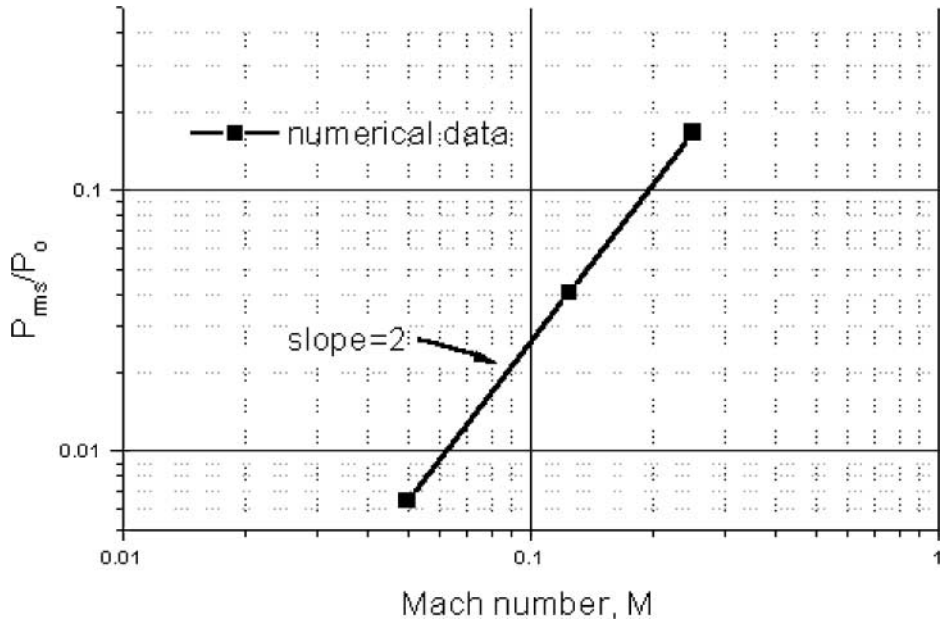

FIG. 19. Finite scattering at the axis of symmetry behind the vortex versus Mach number for $\delta = 4$.

Figs. 14, 16, and 17. These phenomena were also observed in DNS of the Navier–Stokes equations in [20]. As discussed in this study, the discrepancy between theory and numerics can be attributed to the inhomogeneity of density in the compressible vortex, which results in additional scattering effects. This effect must be of $O(M_v^2)$ as the Mach number decreases. Therefore, it should be expected that the finite scattering at $\varphi = 0$ vanishes as M_v^2 when the Mach number tends to zero. This was supported by the DNS of [20] by a logarithmic plot of the far-field pressure amplitude of the scattered waves at $\varphi = 0$ versus M_v; the data were found to have a straight-line trend with a slope of 2. Similar data obtained from the present calculations are plotted in Fig. 19, which also indicates that the scaling with M_v^2 holds.

6.2. Incidence of Two-Dimensional Sound Waves on a Shock Wave

Another example application of the present numerical approach is the simulation of the propagation of two-dimensional sound waves across a shock wave. The statement of this problem is quite similar to that relating to the normal incidence of sound on a shock, which was considered in the previous section. The computational domain is a box with dimensions H and $2H$ on the vertical and horizontal sides, respectively, where the height H is taken as $H = 4$ in nondimensional units. The base flow consists of two uniform flows upstream and downstream of a stationary plane shock wave located at the middle of the domain normal to the streamwise direction. The shock Mach number is set at $M_{sh} = 1.2$.

The acoustic field is generated by two sources of sound, which are symmetrically arranged upstream at the bottom and top boundaries. Each source is a vibrator (or speaker) that is represented by a short rigid plate executing small harmonic oscillations in the direction transverse to the base stream. The velocity of the vibration is given as $U_{sp} = U_0 \cos(\omega t)$, with ω being the frequency of oscillation. The length of each vibrator is $0.125H$, and they are placed at a distance $0.03H$ from the left inlet boundary.

This problem is solved by using a uniform grid with 320 cells in the streamwise direction and 160 cells in the transverse direction. All boundaries except for the speaker portion are treated by nonreflecting boundary conditions. Moving-wall boundary conditions are applied for the speaker boundaries.

Results of this calculation are shown in Fig. 20, where the computed sound pressure is presented for several instants after the vibrators start generating sound waves of a frequency $\omega = 4\pi$. At the early stage of this process the sound waves propagate toward each other and are drifted to the shock wave by the base flow. This is displayed in Figs. 20a and 20b. Before interacting with each other, the waves pass through the shock wave with little refraction so that the transmitted waves have almost the same wave pattern as the incident waves, as

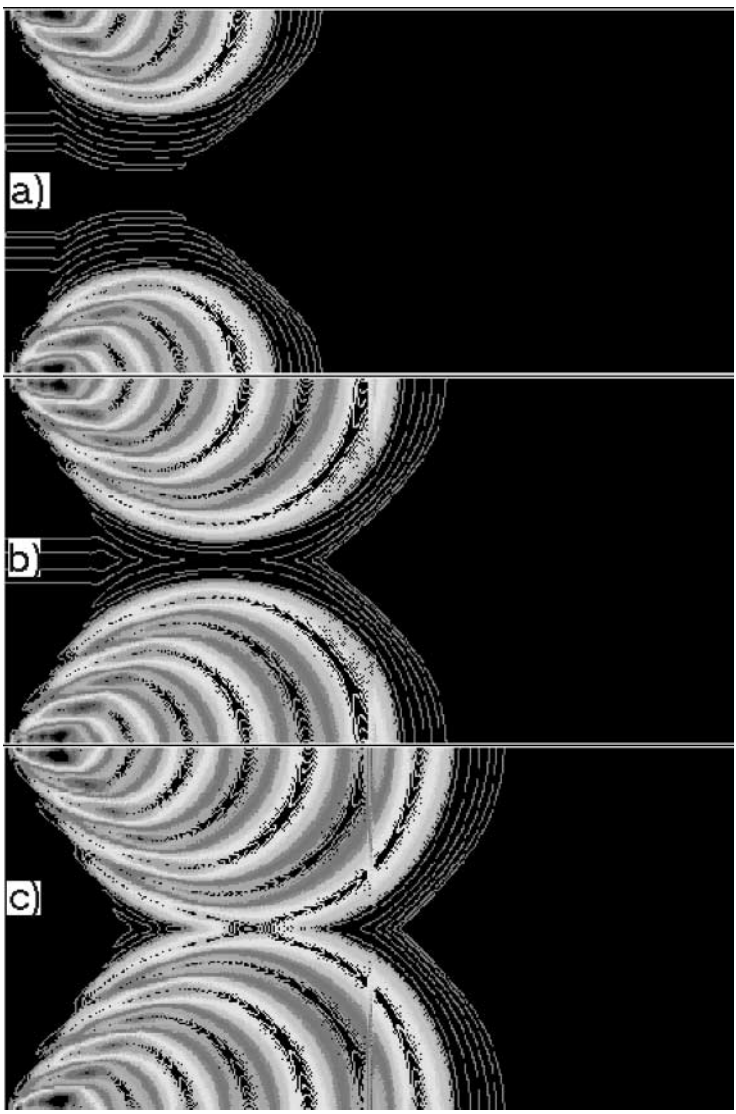

FIG. 20. Time sequence of computed acoustic pressure contours; sound waves are generated by two speakers in the upstream of a shock of $M_{sh} = 1.2$.

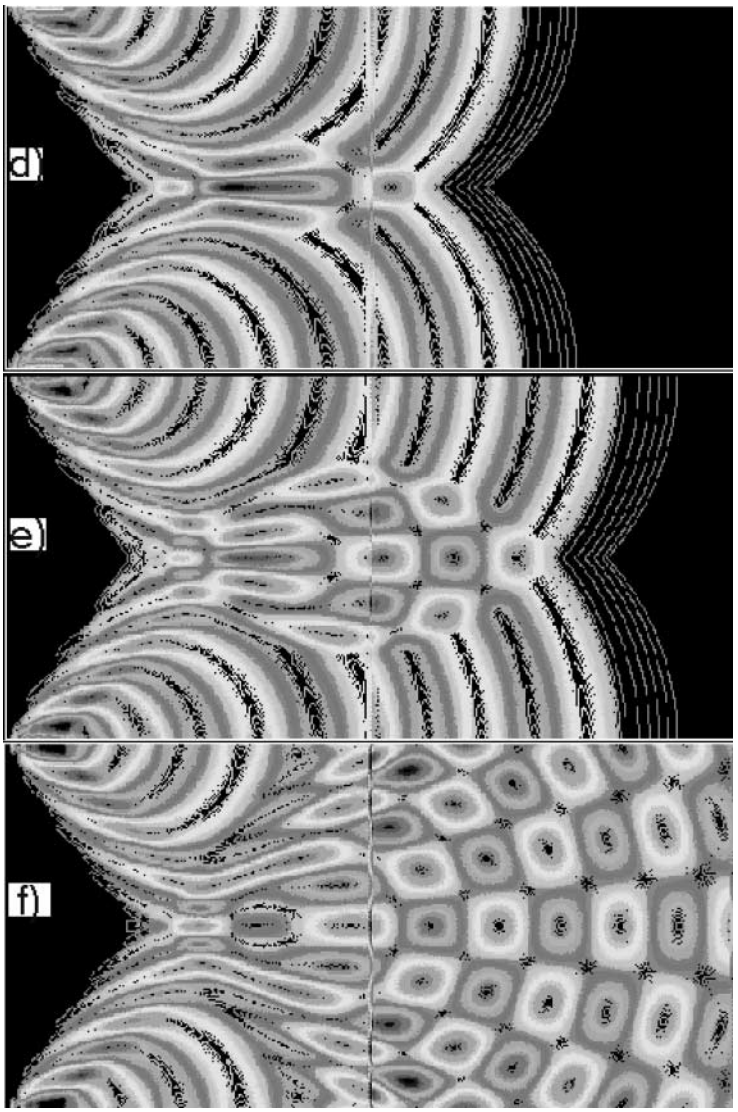

FIG. 20—*Continued*

can be seen in Fig. 20c. When the leading waves reach the centerline of the computational domain, interference occurs between the incident waves, which is shown in Figs. 20d and 20e. This modifies the wave pattern behind the shock wave, which takes on a certain regular cellular structure as shown in Fig. 20f.

7. CONCLUSIONS

A Godunov-type method has been proposed for computing propagation of acoustic disturbances in nonuniform flows. This method can be thought of as a direct extension of the Godunov second-order scheme for computational fluid dynamics to the acoustic equations. A key point of the method is the use of the exact solution to the variational Riemann problem,

which also can be recognized as the problem of interaction between two elementary disturbances, to obtain the acoustic numerical flux. The solution to the VRP is represented in terms of variation matrices associated with the left- and right-hand-side initial disturbance data. Exact formulas for these matrices have been analytically derived in explicit compact form. Validation tests have been carried out to examine whether the proposed approach can handle wave-type solutions. Calculations have been performed for several problems that have exact analytical solutions: acoustic fields generated by monopole and dipole sources and normal and oblique incidence of sound waves on a shock wave. The numerical and analytical solutions have been found to be in good quantitative agreement. Example calculations have shown the ability of the present method to accurately compute scattering of sound by smooth vortical flows and propagation of sound waves in flow with a shock wave.

The results and test cases in the present paper demonstrate the capabilities of the two-dimensional version of the method on structured grids. Extension of the method to three dimensions and unstructured grids appears promising; at least the application of the VRP solution to these cases is straightforward. However, extensive validation of the method implemented on 3-D unstructured grids is required, which will be done in our future work.

REFERENCES

1. S. K. Godunov, A difference scheme for numerical computation of discontinuous solution of hydrodynamic equations, *Math. Sb.* **47**, 271 (1959) [in Russian]; translation, U.S. Joint Publ. Res. Service, JPRS 7226 (1969).
2. N. E. Kochin, *Collected Papers, II* (Akademia Nauk SSSR, Moscow, 1949), pp. 5–42 [in Russian].
3. B. E. Mitchell, S. K. Lele, and P. Moin, Direct computation of the sound from a compressible co-rotating vortex pair, *J. Fluid Mech.* **285**, 181 (1995).
4. O. Inoue and Y. Hattori, Sound generation by shock-vortex interactions, *J. Fluid Mech.* **380**, 81 (1999).
5. Y. Nakamura and H. Yamaguchi, Compressible jet and its sound emission, *Comp. Fluid Dyn. J.* **8**, 250 (1999).
6. T. Furukawa and Y. Nakamura, *Numerical Simulation of Detailed Underexpanded Jet Structure and Its Noise Emission* (electronic publication of the 14th CFD Symposium: http://www.soc.nacsis.ac.jp/jscfd/cfds14/cfds14.html, A08-2, 2000) [in Japanese].
7. C. Y. Loh, L. S. Hultgren, X. Y. Wang, S.-C. Chang, and P. Jorgenson, *Aeroacoustics Computation for Nearly Fully Expanded Supersonic Jets Using the CE/SE Method*, Technical Paper 2000-2010 (AIAA Press, Washington, DC, 2000).
8. R. R. Mankbadi, R. Hixon, S.-H. Shin, and L. A. Povinelli, Use of linearized Euler equations for supersonic jet noise prediction, *AIAA J.* **36**, 140 (1998).
9. T. A. Manning and S. K. Lele, *A Numerical Investigation of Sound Generation in Supersonic Jet Screech*, Technical Paper 2000-2081 (AIAA Press, Washington, DC, 2000).
10. C. Bailly, C. Bogey, and D Juvé, *Computation of Flow Noise Using Source Terms in Linearized Euler's Equations*, Technical Paper 2000-2047 (AIAA Press, Washington, DC, 2000).
11. K. Viswanathan and L. N. Sankar, Towards the direct calculation of noise: Fluid/acoustics coupled simulation, *AIAA J.* **33**, 2271 (1995).
12. S. K. Godunov, A. V. Zabrodin, M. I. Ivanov, A. N. Kraiko, and G. P. Prokopov, *Résolution numerique des problémes multidimensionnels de la dynamique des gas* (Mir, Moscow, 1979) [in French].
13. I. Men'shov and Y. Nakamura, On implicit Godunov's method with exactly linearized numerical flux, *Comput. Fluids* **29**, 595 (2000).
14. A. Antonov and T. Kozubskaya, *Acoustic Noise Simulation for Supersonic Viscous Compressible Gas Flow*, Computational Fluid Dynamics'98—Proceedings of the 4th European CFD Conference, I, p. 48 (1998).
15. B. van Leer, Toward the ultimate conservative difference scheme, II, *J. Comput. Phys.* **14**, 361 (1979).

16. V. P. Kolgan, Application of the principle of minimum derivative value to the construction of finite-difference schemes for computing discontinuous solutions of gas dynamics, *Uch. Zap. TSAGI* **3**, 68 (1972) [in Russian].
17. L. D. Landau and E. M. Lifshitz, *Fluid Mechanics* (Pergamon, Elmsford, NY, 1982).
18. J. Brillouin, Réflexion et réfraction d'ondes acoustiques par une onde de choc, *Acustica* **5**, 149 (1955) [in French].
19. V. M. Kontorovich, Reflection and refraction of sound by a shock wave, *Sov. Phys. JETP* **33**, 1180 (1958).
20. T. Colonius, S. K. Lele, and P. Moin, The scattering of sound waves by a vortex: Numerical simulations and analytical solutions, *J. Fluid Mech.* **260**, 271 (1994).
21. R. Berthet, D. Astruc, and J. L. Estivalézes, *Assessment of Numerical Boundary Conditions for Simulation of Sound Scattering by Vorticity*, Technical Paper 2000-2005 (AIAA Press, Washington, DC, 2000).
22. R. Ford and S. G. Llewellyn Smith, Scattering of acoustic waves by a vortex, *J. Fluid Mech.* **386**, 305 (1999).
23. M. S. Howe, Contributions to the theory of aerodynamic sound, with application to excess jet noise and the theory of the flute, *J. Fluid Mech.* **71**, 625 (1975).
24. A. L. Fabricant, Sound scattering by vortex flow, *Sov. Phys. Acoust.* **29**, 2 (1983).
25. R. Ewert, M. Meinke, and W. Schröder, *Aeroacoustic Source Terms for the Linearized Euler Equations*, Technical Paper 2000-2046 (AIAA Press, Washington, DC, 2000).